

# Integrating Conductor Health into Dynamic Line Rating and Unit Commitment under Uncertainty

Geon Roh, *Student Member, IEEE*, and Jip Kim, *Member, IEEE*

**Abstract**—Dynamic line rating (DLR) enables greater utilization of existing transmission lines by leveraging real-time weather data. However, the elevated temperature operation (ETO) of conductors under DLR is often overlooked, despite its long-term impact on conductor health. This paper addresses this issue by 1) quantifying depreciation costs associated with ETO and 2) proposing a Conductor Health-Aware Unit Commitment (CHA-UC) that internalizes these costs in operational decisions. The CHA-UC incorporates a robust linear approximation of conductor temperature and integration of expected depreciation costs due to hourly ETO into the objective function. Case studies on the Texas 123-bus backbone test system using NOAA weather data demonstrate that the proposed CHA-UC model reduces the total cost by 0.8% and renewable curtailment by 84% compared to static line rating (SLR), while conventional DLR operation without risk consideration resulted in higher costs due to excessive ETO. Further analysis of the commitment decisions and the line temperature statistics confirms that the CHA-UC achieves safer line flows by shifting generator commitments. Finally, we examine the emergent correlation between wind generation and DLR forecast errors, and show that CHA-UC adaptively manages this effect by relaxing flows for risk-hedging conditions while tightening flows for risk-amplifying ones.

## NOMENCLATURE

All optimization variables that have been fixed and become parameters are marked with an overline to avoid confusion (e.g., Day-ahead variable  $u_{i,t}$  is fixed in the operation stage and is denoted  $\bar{u}_{i,t}$  in the real-time optimization problem).

### Sets and Indices

$b \in \mathcal{B}$	Set of buses.
$l \in \mathcal{L}$	Set of all transmission lines where $\mathcal{L}^{\text{DLR/SLR}}$ denote sets of DLR/SLR applied lines
$i \in \mathcal{I}$	Set of thermal generating units.
$o \in \mathcal{O}_i$	Set of startup segments for unit $i$ .
$w \in \mathcal{W}_b$	Set of wind farms connected at bus $b$ .
$t \in \mathcal{T}$	Set of dispatch time periods.
$s \in \mathcal{S}$	Set of uncertainty scenarios.
$s(l), r(l)$	Sending- and receiving-end buses of line $l$ .

### Parameters

$A_{l,t}, B_{l,t}$	Slope and intercept of linear fit of loading-temperature for line $l$ [ $^{\circ}\text{C}/\text{MW}$ , $^{\circ}\text{C}$ ].
$\hat{A}_{l,t}, \hat{B}_{l,t}$	DA forecast of slope and intercept of the linear fit for line $l$ at time $t$ [ $^{\circ}\text{C}/\text{MW}$ , $^{\circ}\text{C}$ ].
$C_{l,t}^{\text{Dep}}(\cdot)$	Line depreciation cost function [\$/ $^{\circ}\text{C}$ ].
$C_i^{\text{P}}(\cdot)$	Quadratic fuel cost function [\$/MWh].
$C_i^{\text{r}+}, C_i^{\text{r}-}$	Up and down-reserve costs [\$/MWh].
$C_{i,o}^{\text{SU}}, C_i^{\text{SD}}$	Startup and shutdown costs [\$/MWh].

$C^{\text{VOLL}}$	Value of lost load [\$/MWh].
$\underline{F}_l^{\text{SLR}}, \bar{F}_l^{\text{SLR}}$	SLR of line $l$ [MW].
$\underline{F}_l^{\text{DLR}}, \bar{F}_l^{\text{DLR}}$	RT DLR of line $l$ , time $t$ [MW].
$\hat{F}_l^{\text{DLR}}, \bar{F}_l^{\text{DLR}}$	DA DLR forecasts of line $l$ , time $t$ [MW].
$\underline{G}_i, \bar{G}_i$	Minimum, maximum power output [MW].
$P_{b,t}^{\text{d}}$	Load at bus $b$ and time $t$ [MW].
$P_{w,t}^{\text{wind}}$	RT WP generation [MW].
$\hat{P}_{w,t}^{\text{wind}}$	DA Forecast WP generation [MW].
$\Pr_s$	Probability of scenario $s$ .
$R_t^{\text{min},+}$	Required system total up reserve.
$RU_i, RD_i$	Ramp-up and ramp-down limits [MW/h].
$SU_i, SD_i$	Startup and shutdown capability [MW].
$T_{i,o}^{\text{SU}}$	Hours defining the segment $o$ limits [h].
$TU_i, TD_i$	Minimum up- and down-times of unit $i$ [h].
$X_l$	Reactance of line $l$ [p.u.].
$\Theta_l, \bar{\Theta}_l$	Phase-angle difference limits on line $l$ [rad].
$\xi_{l,t,s}$	DLR forecast error scenario $s$ [MW].
$\omega_{w,t,s}$	WP forecast error scenario $s$ [MW].
$K_{l,t}$	DLR security margin multiplier.

### Variables

$g_{i,t}$	DA dispatch of unit $i$ at time $t$ [MW].
$\hat{g}_{i,t,s}, g_{i,t}^{\text{adj}}$	DA and RT adjusted generation of unit $i$ at time $t$ [MW].
$p_{l,t}$	DA power flow on line $l$ at time $t$ [MW].
$\hat{p}_{l,t,s}, p_{l,t}^{\text{adj}}$	DA and RT adjusted power flow of line $l$ at time $t$ [MW].
$p_{w,t}^{\text{cur}}$	DA wind generation curtailment [MW].
$\hat{p}_{w,t,s}^{\text{cur,adj}}, p_{w,t}^{\text{cur,adj}}$	DA and RT adjusted wind generation curtailment at farm $w$ , time $t$ [MW].
$\hat{p}_{b,t}^{\text{shed}}$	DA load shedding at bus $b$ , time $t$ [MW].
$\hat{p}_{b,t,s}^{\text{shed,adj}}, p_{b,t}^{\text{shed,adj}}$	DA and RT adjusted load shedding at bus $b$ , time $t$ [MW].
$r_{i,t}^{\text{avail},+}$	DA available online up reserve [MW].
$\hat{r}_{i,t,s}^+, \hat{r}_{i,t,s}^-$	DA up and down-reserve activation given scenario $s$ for unit $i$ , time $t$ , [MW].
$r_{i,t}^+, r_{i,t}^-$	RT up and down-reserve activation for unit $i$ , time $t$ , [MW].
$u_{i,t}$	Binary commitment variable
$u_{i,t}^{\text{SU}}, u_{i,t}^{\text{SD}}$	Binary startup/shutdown variable.
$\delta_{i,o,t}$	Activation of startup-segment $o$ .
$\theta_{b,t}$	DA voltage angle [rad].
$\hat{\theta}_{b,t,s}^{\text{adj}}, \theta_{b,t}^{\text{adj}}$	DA and RT adjusted voltage angle [rad].
$\hat{\tau}_{l,t,s}$	DA conductor temperature given scenario $s$ on line $l$ , time $t$ [ $^{\circ}\text{C}$ ].
$\tau_{l,t}$	RT temperature of conductor [ $^{\circ}\text{C}$ ].

## I. INTRODUCTION

The large-scale integration of renewable energy sources (RES) into power systems remains a major technical challenge, particularly due to the spatial mismatch between high-potential generation sites and demand centers. Areas with high RES potential are far from demand, and efficient RES integration plans entail intense transmission expansion [1]. Case studies in Texas indicate that transmission expansion costs rise significantly when RES are integrated due to their remote locations [2]. Moreover, transmission construction lags generation: wind and solar projects can be built within three years, whereas new transmission requires five to ten years [3], [4]. This mismatch causes grid congestion, increased operation costs, and curtailed renewable generation. For instance, in 2024, 4% of WP generation and 6% of solar generation were curtailed in Texas [5], while in Korea, four out of ten RES producers could not connect to the grid, causing an estimated \$6.7 billion in losses [6]. Given these challenges, maximizing the use of existing transmission lines is essential for RES integration.

Dynamic line rating (DLR) has emerged as a promising solution that exploits real-time weather conditions to increase the utilization of existing transmission facilities. For overhead transmission lines under 100 km, the transmission capacity is mostly restricted by its thermal limits. Unlike static line rating (SLR), which assumes conservative worst-case weather conditions (e.g., 0.5 m/s wind speed, 40°C ambient temperature), DLR adjusts ampacity dynamically. The synergy with wind power is particularly strong, as both depend on wind speed, a spatially correlated factor. Authors of [7] and [8] both prove that applying DLR is effective in reducing WP curtailment. Especially, [8] shows that the system operator may save 776 M\$ per year from congestion costs in Texas by introducing DLR. Federal Energy Regulatory Commission (FERC) is working to advance its framework on DLR. In 2024, FERC issued an Advance Notice of Proposed Rulemaking (ANOPR) related to DLR [9]. This ANOPR builds on Order 881 [10], detailing the addition of wind and solar factors to ambient-adjusted ratings.

DLR, however, poses risks of sag and accelerated conductor degradation, especially under elevated temperature operation (ETO). Moreover, the correlation between wind generation and DLR forecasts can amplify risk. This risk was not considered in [7] and [8]. Prior work has attempted to address forecast uncertainty using chance-constrained OPF [11], Gaussian copulas [12], or distributionally robust formulations [13]. Park et al. [14] extended this to stochastic unit commitment, showing that commitment decisions differ under SLR and DLR. Other works proposed risk-averse forecasts using quantile or super-quantile regression [15]. In the actual world, FERC requires a quantile forecast value with a confidence level of 98%, meaning that the actual value of DLR should be greater than the forecast value 98% of the time [9]. The authors of [16] obtain quantile forecast values of DLR using a graph convolutional long short-term memory model.

Despite these advances, existing models do not account for the actual costs of ETO, even though ETO occurs under both SLR and DLR [17]. Without quantifying ETO-induced

depreciation, models remain mathematically robust but economically incomplete. Previous works have handled the effect of ETO, and some have expanded it to DLR, but no works have integrated ETO costs into decision making such as OPF or UC. Harvey's seminal work [18] modeled the effect of ETO on aluminum conductors through an empirical equation for tensile strength loss (LoTS) as a function of conductor temperature and elapsed time. This model has been widely adopted to model ETO, including Musilek et al. [19], EPRI [20] and PJM [21]. [19] analyzed the historical aging of a conductor using meteorological data. Moreover, [22] modeled the risk of DLR using the LoTS model and conducted a sensitivity analysis. However, this research does not consider the actual operation and performs only a simple calculation based on one line. Other depreciation models, such as fretting-based reliability analysis [23], rely on strong assumptions with limited empirical support. To the best of our knowledge, no existing optimization framework integrates realistic conductor health costs into OPF or UC formulations.

Incorporating ETO into optimization requires embedding a conductor temperature estimation model. However, because external climate conditions are highly dynamic, and the current-temperature relationship is multimodal (affected by many weather components) and nonlinear, direct integration into optimization is impractical. Previous studies have proposed conductor temperature models within OPF formulations [15], [24], [25]. While these works employ current-temperature proxies, they do not capture the consequences of ETO, leaving a key gap in the literature. In addition, most adopt day-ahead quadratic fits of the current-temperature relationship, which present two drawbacks: (i) they can become computationally intensive when combined with stochastic optimization, and (ii) they may underestimate conductor temperature, undermining risk management.

This paper addresses this gap by developing a day-ahead stochastic UC model that accounts for (i) DLR operation, (ii) power system uncertainties, and (iii) the long-term costs of ETO. Incorporating ETO costs is challenging due to the state dependency of conductor depreciation models and the lack of a closed-form solution to the loading-temperature relationship. To overcome these challenges, we introduce a piecewise linear conductor depreciation cost function and a linear line loading-temperature proxy. The main contributions of this paper are as follows:

- 1) *Modeling of ETO effects:* We develop tractable models to capture the long-term effects of elevated temperature operation (ETO), including (i) a robust and computationally efficient line loading-temperature proxy, and (ii) a piecewise conductor depreciation cost function.
- 2) *Conductor Health-Aware Unit Commitment (CHA-UC):* Building on these models, we formulate a stochastic UC framework that internalizes conductor health costs in operational decision making, explicitly balancing conductor depreciation against system operating costs.
- 3) *Validation on a realistic test system:* We evaluate the CHA-UC on the synthetic Texas 123-bus backbone test system (TX-123BT) under multiple sources of uncertainty. Results highlight differences in commitment deci-

sions, demonstrate improved handling of DLR risks, and show that CHA-UC effectively addresses the correlation between wind generation and DLR forecast errors.

## II. CONDUCTOR COST DEPRECIATION MODEL

This section quantifies the long-term effects of elevated conductor temperature operation (ETO) and formulates a depreciation model suitable for optimization.

### A. Heat balance equation

The steady-state heat balance equation (HBE) [26] is used to obtain the DLR and corresponding conductor temperature. Since our focus is on hour-scale unit commitment, transient effects are neglected: the conductor reaches 95% of the steady-state value within approximately 42 minutes [14]. The steady-state HBE is expressed as:

$$q_c + q_r = q_s + I^2 R(\tau_{avg}) \quad (1)$$

where  $q_c$ ,  $q_r$ , and  $q_s$  denote convective and radiative heat losses and solar heat gain, respectively, and  $I^2 R(\tau_{avg})$  is the Joule heating term. Among these, wind speed has the strongest influence on the DLR, followed by ambient temperature and solar radiation [7].

### B. Linear temperature approximation

The current-temperature relationship is convex under realistic operating conditions, as confirmed through parametric sweeps of an ACSR Finch conductor (current: 500–3500 A, wind speed: 0–8 m/s, ambient temperature: 0–45 °C). Concave regions appear only for extreme overheating ( $\tau \geq 350$  °C, wind speed  $\leq 2$  m/s), which are beyond the safe operating range for ACSR. Thus, a linear approximation provides a conservative and computationally efficient proxy. Figure 1 shows the linear fit of the HBE-derived temperature curve. Within the emergency loading range (100–150% of rated current [27]), the linear proxy yields a mean absolute error of 0.7% and a maximum error of 2.2%. Because the function is convex, the linearization is constructed to slightly overestimate temperature, ensuring conservativeness.

This loading-temperature relationship can be embedded in optimization problems including the DC power flow (PF) equation. The constraints are formulated as ( $\forall l \in \mathcal{L}, t \in \mathcal{T}$ ):

$$\tau_{l,t} \geq A_{l,t} \cdot p_{l,t} + B_{l,t}, \quad (2a)$$

$$\tau_{l,t} \geq -A_{l,t} \cdot p_{l,t} + B_{l,t}, \quad (2b)$$

where  $p_{l,t}$  is the line power flow. Because voltage is assumed constant in DC power flow,  $A_{l,t}$  is scaled by  $\frac{1}{\sqrt{3}V_l^{\text{Nom}}}$  from the current-temperature fit. The two inequalities account for bidirectional flow, ensuring  $\tau_{l,t}$  is an upper bound on the actual conductor temperature.

### C. Loss of tensile strength (LoTS) for ACSR lines

Long-term ETO causes conductor degradation, measured as the loss of tensile strength (LoTS). For aluminum strands, LoTS (%) is empirically modeled as [18]:

$$L_{\text{AI}} = 100 - A t^{-\frac{25.4}{d}} (0.001\tau - 0.095), \quad (3)$$

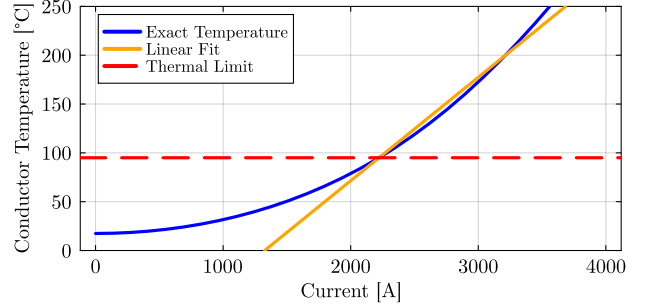


Fig. 1: Illustration of a linear fit to the current-conductor temperature relationship. The temperature from the IEEE HBE and the linear fit assuming ACSR Finch, a perpendicular wind speed of 2.7 m/s and ambient temperature of 9.4°C is shown. Conductor temperature limit is set as 95 °C; in practice, it varies depending on the transmission system owner [28].

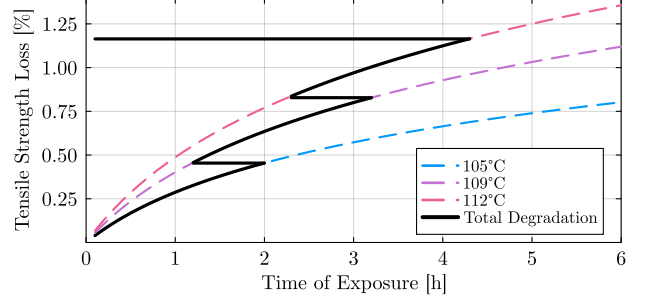


Fig. 2: An illustrative example of LoTS with a conductor with exposed temperatures: 105°C, 109°C, 112°C each for two hours. The path of total degradation calculation is shadowed on trajectories of different temperatures [19].

where  $A = \min(100, 134 - 0.24\tau)$ ,  $\tau$  is conductor temperature (°C),  $t$  is exposure time (h), and  $d$  is conductor diameter (mm). For aluminum conductor steel-reinforced (ACSR) lines, the corresponding LoTS is approximated as [19]:

$$L_{\text{ACSR}} = 0.735 L_{\text{AI}}. \quad (4)$$

The accumulated LoTS is obtained by integrating temperature exposure over time, enabling direct quantification of ETO-induced degradation. Figure 2 illustrates the calculation process using temperature-time exposure pairs ordered from low to high temperature. At each step, prior exposures are converted into an equivalent time at the current (higher) temperature, added to the new exposure, and the remaining tensile strength is updated via the LoTS model. Repeating this process yields the total LoTS at the highest temperature.

### D. Piecewise depreciation cost for overhead lines

Operation of ACSR lines beyond 95°C accelerates tensile strength loss; thus, LoTS can be translated into economic depreciation. The ratio of the accumulated LoTS to an end-of-life value (typically 10% [17], [29]) represents the remaining conductor value. The cost of one hour ETO at a given temperature is calculated by incorporating the capital cost of a transmission line into a linear depreciation model. When the LoTS limit is reached, the line is assumed to lose its value. The depreciation is calculated as follows:

$$C_{l,t}^{\text{Dep}}(\tau) = B_l \cdot S_l \cdot D_l \cdot \frac{L_{\text{ACSR},t}(\tau) - L_{\text{ACSR},t-1}}{10}, \quad (5)$$

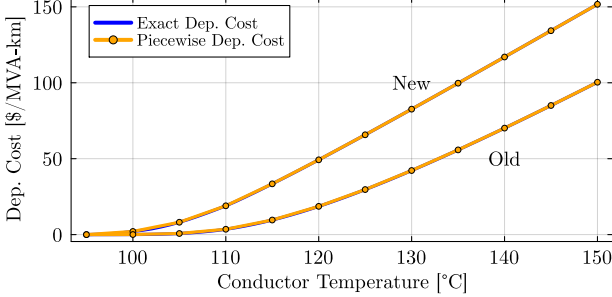


Fig. 3: Depreciation cost piecewise functions for new and old ACSR Finch. The piecewise functions lay above the exact depreciation cost.

where  $B_l$  is the initial cost factor of line  $l$  (\$/MVA-km),  $S_l$  its capacity (MVA), and  $D_l$  its length (km). Subscript  $t$  denotes the time of interest. This formulation implies that  $C_t^{\text{Dep}}(\tau)$  varies with the state of the conductor as  $L_{\text{ACSR},t}(\cdot)$  is state-dependent. While the depreciation model in (5) can be applied in post-hoc evaluation, this research aims to integrate it into the UC problem with DLR which involves the real-time decision-making. Thus, we approximate the expected cost of a one-hour ETO by formulating the 1-hour ETO costs at different temperatures as a piecewise function prior to solving the daily CHA-UC problem. This function is convex, as higher temperature yield steeper depreciation slopes, and is calculated separately for each conductor. Figure 3 depicts the depreciation cost function and its piecewise counterpart for an old transmission line with many ETO histories (old) and a transmission line with less ETO histories (new).

### III. CONDUCTOR HEALTH-AWARE UNIT COMMITMENT

Adopting DLR pushes line temperatures toward thermal limits, amplifying ETO risk in the presence of forecast errors. We propose the CHA-UC framework, which minimizes the sum of expected conductor depreciation and system operating costs to balance reliability and economics. This enables the system operator to provide the most effective commitment decisions and dispatch, using DLR.

#### A. Baseline UC model

Before presenting the CHA-UC framework, the deterministic baseline model for DLR and SLR is introduced. Day-ahead UC and real-time operation is reflected in the model. The UC problem fixes commitment decisions day before the actual operation, using day-ahead forecasts and considering physical constraints of generators. The enforcement of UC constraints lead to a more comprehensive benchmark of results [14]. The operation step adjusts the generation of available generators under ramping constraints and fixed commitments to account forecast error.

The objective function of the day-ahead UC problem is:

$$\begin{aligned} \min_{\Xi} \quad & \sum_{t \in \mathcal{T}} \sum_{i \in \mathcal{I}} \left[ u_{i,t} \cdot C_i^{\text{P}}(g_{i,t}) + \sum_{o \in \mathcal{O}_i} \delta_{i,o,t} \cdot C_{i,o}^{\text{SU}} \right. \\ & \left. + u_{i,t}^{\text{SD}} \cdot C_i^{\text{SD}} \right] + \sum_{t \in \mathcal{T}} \sum_{b \in \mathcal{B}} C^{\text{VoLL}} p_{b,t}^{\text{shed}}, \end{aligned} \quad (6)$$

which is the sum of production cost, startup cost and the shut down cost.  $\Xi := \{\mathbf{g}, \mathbf{p}, \mathbf{u}, \boldsymbol{\theta}, \boldsymbol{\delta}\}$

The day-ahead UC constraints, hereafter referred to as the UC constraints, are adapted from the formulation of Morales-España et al. [30]:

$$\delta_{i,o,t} \leq \sum_{k=T_{i,o}^{\text{SU}}}^{T_{i,o+1}-1} u_{i,t-k}^{\text{SD}}, \quad \forall i \in \mathcal{I}, t \in [T_{i,o+1}, T], o \in [1, O_i], \quad (7a)$$

$$\sum_{o \in \mathcal{O}_i} \delta_{i,o,t} = u_{i,t}^{\text{SU}} \quad \forall i \in \mathcal{I}, t \in \mathcal{T}, \quad (7b)$$

$$\sum_{k=t-TU_i+1}^t u_{i,k}^{\text{SU}} \leq u_{i,t}, \quad \forall i \in \mathcal{I}, t \in [TU_i, T], \quad (7c)$$

$$\sum_{k=t-TD_i+1}^t u_{i,k}^{\text{SD}} \leq 1 - u_{i,t}, \quad \forall i \in \mathcal{I}, t \in [TD_i, T], \quad (7d)$$

$$u_{i,t} - u_{i,t-1} = u_{i,t}^{\text{SU}} - u_{i,t}^{\text{SD}}, \quad \forall i \in \mathcal{I}, t \in \mathcal{T}, \quad (7e)$$

$$g_{i,t} \leq (\bar{G}_i - \underline{G}_i) u_{i,t} - (\bar{G}_i - SU_i) u_{i,t}^{\text{SU}}, \quad \forall i \in \mathcal{I}^1, t \in \mathcal{T}, \quad (7f)$$

$$g_{i,t} \leq (\bar{G}_i - \underline{G}_i) u_{i,t} - (\bar{G}_i - SD_i) u_{i,t+1}^{\text{SD}}, \quad \forall i \in \mathcal{I}^1, t \in \mathcal{T}, \quad (7g)$$

$$\begin{aligned} g_{i,t} \leq (\bar{G}_i - \underline{G}_i) u_{i,t} - (\bar{G}_i - SU_i) u_{i,t}^{\text{SU}} \\ - (\bar{G}_i - SD_i) u_{i,t+1}^{\text{SD}}, \quad \forall i \in \mathcal{I} \setminus \mathcal{I}^1, t \in \mathcal{T}, \end{aligned} \quad (7h)$$

$$g_{i,t} - g_{i,t-1} \leq RU_i \quad \forall i \in \mathcal{I}, t \in \mathcal{T}, \quad (7i)$$

$$- g_{i,t} + g_{i,t-1} \leq RD_i \quad \forall i \in \mathcal{I}, t \in \mathcal{T}. \quad (7j)$$

Startup and shutdown costs are modeled by (7a)–(7b), and minimum up/down times by (7c)–(7d). The logical constraint (7e) links the binary variables, while (7f)–(7h) enforce generation limits ( $\mathcal{I}^1$  denotes units with  $TU_i = 1$ ). Ramping limits are imposed by (7i) and (7j).

Supplementary constraints for the day-ahead UC are:

$$p_{l,t} = \frac{1}{X_l} (\theta_{s(l),t} - \theta_{r(l),t}), \quad \forall l \in \mathcal{L}, t \in \mathcal{T}, \quad (8a)$$

$$\begin{aligned} \sum_{l|s(l)=b} p_{l,t} - \sum_{l|r(l)=b} p_{l,t} + \sum_{i \in \mathcal{I}_b} g_{i,t} + \sum_{w \in \mathcal{W}_b} (\hat{P}_{w,t}^{\text{wind}} - p_{w,t}^{\text{cur}}) \\ = P_{b,t}^{\text{d}} - p_{b,t}^{\text{shed}}, \quad \forall b \in \mathcal{B}, t \in \mathcal{T}, \end{aligned} \quad (8b)$$

$$p_{w,t}^{\text{cur}} \leq \hat{P}_{w,t}^{\text{wind}}, \quad \forall w \in \mathcal{W}, t \in \mathcal{T} \quad (8c)$$

$$r_{i,t}^{\text{avail},+} \leq R_i^{\text{RU}} u_{i,t}, \quad \forall i \in \mathcal{I}, t \in \mathcal{T}, \quad (8d)$$

$$r_{i,t}^{\text{avail},+} \leq \bar{P}_i - g_{i,t}, \quad \forall i \in \mathcal{I}, t \in \mathcal{T}, \quad (8e)$$

$$\sum_{i \in \mathcal{I}} r_{i,t}^{\text{avail},+} \geq R_t^{\text{min},+}, \quad \forall t \in \mathcal{T}, \quad (8f)$$

$$F_l^{\text{SLR}} \leq p_{l,t} \leq \bar{F}_l^{\text{SLR}}, \quad \forall l \in \mathcal{L}^{\text{SLR}}, t \in \mathcal{T}, \quad (8g)$$

$$K_{l,t} \hat{F}_{l,t}^{\text{DLR}} \leq p_{l,t} \leq K_{l,t} \bar{F}_{l,t}^{\text{DLR}}, \quad \forall l \in \mathcal{L}^{\text{DLR}}, t \in \mathcal{T}. \quad (8h)$$

The network is modeled with DC power flow (8a), and nodal balance is enforced by (8b). Equations (8c)–(8f) impose wind curtailment and reserve requirements. Angle and flow envelopes (8g)–(8h) ensure grid security, where  $K_{l,t} \in [0, 1]$  is the operator-defined DLR margin.

Once the day-ahead dispatch is fixed, the real-time operation minimizes the additional cost of balancing actual wind

generation and DLR realizations:

$$\begin{aligned} \min_{\Xi} \sum_{t \in \mathcal{T}} \sum_{i \in \mathcal{I}} & \left[ C_i^{\text{P},2}(g_{i,t}^{\text{adj}})^2 + C_i^{\text{r}+} r_{i,t}^+ + C_i^{\text{r}-} r_{i,t}^- \right] \\ & + \sum_{t \in \mathcal{T}} \sum_{b \in \mathcal{B}} C^{\text{VoLL}} p_{b,t}^{\text{shed,adj}}, \end{aligned} \quad (9)$$

where  $\Xi := \{\mathbf{g}^{\text{adj}}, \mathbf{p}^{\text{adj}}, \mathbf{r}^{+,-}, \boldsymbol{\theta}^{\text{adj}}\}$ . Reserve activations are penalized through  $C_i^{\text{r}\pm}$ , and the quadratic term captures nonlinear production costs. This objective represents the operator's total adjustment cost in real time. The constraints of the operation stage are as follows:

$$g_{i,t}^{\text{adj}} = \bar{g}_{i,t} + r_{i,t}^+ - r_{i,t}^-, \quad \forall i \in \mathcal{I}, t \in \mathcal{T}, \quad (10a)$$

$$0 \leq r_{i,t}^+ \leq \bar{u}_{i,t} \cdot G_i^{\text{RU}}, \quad \forall i \in \mathcal{I}, t \in \mathcal{T}, \quad (10b)$$

$$0 \leq r_{i,t}^- \leq u_{i,t} \cdot G_i^{\text{RD}}, \quad \forall i \in \mathcal{I}, t \in \mathcal{T}, \quad (10c)$$

$$\underline{G}_i \leq g_{i,t}^{\text{adj}} \leq \bar{G}_i, \quad \forall i \in \mathcal{I}, t \in \mathcal{T}, \quad (10d)$$

$$p_{l,t}^{\text{adj}} = \frac{1}{X_l} (\theta_{s(l),t}^{\text{adj}} - \theta_{r(l),t}^{\text{adj}}), \quad \forall l \in \mathcal{L}, t \in \mathcal{T}, \quad (10e)$$

$$\sum_{l|s(l)=b} p_{l,t}^{\text{adj}} - \sum_{l|r(l)=b} p_{l,t}^{\text{adj}} + \sum_{i \in \mathcal{I}_b} g_{i,t}^{\text{adj}} + \sum_{w \in \mathcal{W}_b} (P_{w,t}^{\text{wind}} - p_{w,t}^{\text{cur,adj}}) = P_{b,t}^{\text{d}} - p_{b,t}^{\text{shed,adj}}, \quad \forall b \in \mathcal{B}, t \in \mathcal{T}, \quad (10f)$$

$$p_{w,t}^{\text{cur,adj}} \leq P_{w,t}^{\text{wind}}, \quad \forall w \in \mathcal{W}, t \in \mathcal{T}. \quad (10g)$$

The real-time operation balances supply and demand under fixed commitment decisions by activating reserves and adjusting wind curtailment and load shedding. Day-ahead dispatch is corrected through up- and down-reserve activation as defined in (10a), subject to ramping, generation, and commitment constraints (10b)–(10d). The real-time power balance (10f) is updated to reflect actual wind generation and the adjusted power flows, generation, and curtailment.

### B. Conductor health-aware unit commitment

Given the linear fit and the piecewise depreciation cost function in Section II, the objective function of the CHA-UC day-ahead problem is as follows:

$$\begin{aligned} \min_{\Xi} \sum_{t \in \mathcal{T}} \sum_{i \in \mathcal{I}} & \left[ C_i^{\text{P}}(g_{i,t}) u_{i,t} + \sum_{o \in \mathcal{O}_i} C_{i,o}^{\text{SU}} \delta_{i,o,t} + C_i^{\text{SD}} u_{i,t} \right] \\ & + \sum_{t \in \mathcal{T}} \sum_{b \in \mathcal{B}} C^{\text{VoLL}} p_{b,t}^{\text{shed}} + \sum_{s \in \mathcal{S}} \Pr_s \sum_{t \in \mathcal{T}} \left[ \underbrace{\sum_{l \in \mathcal{L}^{\text{DLR}}} C_{l,t}^{\text{Dep}} (\hat{\tau}_{l,t,s})}_{\text{Expected depreciation cost}} \right. \\ & \left. + \underbrace{\sum_{b \in \mathcal{B}} C^{\text{VoLL}} \hat{p}_{b,t,s}^{\text{shed,adj}}}_{\text{Expected load shedding cost}} + \underbrace{\sum_{i \in \mathcal{I}} [C^{\text{r}+} \hat{r}_{i,t,s}^+ + C^{\text{r}-} \hat{r}_{i,t,s}^-]}_{\text{Expected reserve activation cost}} \right]. \end{aligned} \quad (11)$$

The objective includes the operation cost from (6) and the scenario stochastic costs: the expected conductor depreciation cost, expected load shed costs and the expected reserve activation costs. The decision variables are identical to the baseline. The additional term in (11) represents the expected values from considering stochasticity. The sample average approximation was used to calculate the expected value.  $C_{l,t}^{\text{Dep}}$  is a piecewise function of the depreciation cost of ETO in Section II-D, implemented using **SOS2** constraints.

CHA-UC is constrained by the UC constraints and the DC power flow constraints from the baseline.

$$(7a) - (7j) \quad \text{UC Constraints,} \quad (12a)$$

$$(8a) - (8h) \quad \text{Suppl. Constraints.} \quad (12b)$$

Additional scenario-based stochastic constraints are as follows ( $\forall s \in \mathcal{S}$ ):

$$\hat{g}_{i,t,s}^{\text{adj}} = g_{i,t} + \hat{r}_{i,t,s}^+ - \hat{r}_{i,t,s}^-, \quad \forall i \in \mathcal{I}, t \in \mathcal{T}, \quad (13a)$$

$$0 \leq \hat{r}_{i,t,s}^+ \leq G_i^{\text{RU}}, \quad \forall i \in \mathcal{I}, t \in \mathcal{T}, \quad (13b)$$

$$0 \leq \hat{r}_{i,t,s}^- \leq G_i^{\text{RD}}, \quad \forall i \in \mathcal{I}, t \in \mathcal{T}, \quad (13c)$$

$$\underline{G}_i \leq \hat{g}_{i,t,s}^{\text{adj}} \leq \bar{G}_i, \quad \forall i \in \mathcal{I}, t \in \mathcal{T}, \quad (13d)$$

$$\hat{p}_{l,t,s}^{\text{adj}} = \frac{1}{X_l} (\theta_{s(l),t,s}^{\text{adj}} - \hat{\theta}_{r(l),t,s}^{\text{adj}}), \quad \forall l \in \mathcal{L}, t \in \mathcal{T}, \quad (13e)$$

$$\begin{aligned} \sum_{l|s(l)=b} \hat{p}_{l,t,s}^{\text{adj}} - \sum_{l|r(l)=b} \hat{p}_{l,t,s}^{\text{adj}} + \sum_{i \in \mathcal{I}_b} \hat{g}_{i,t,s}^{\text{adj}} + \sum_{w \in \mathcal{W}_b} (\hat{P}_{w,t}^{\text{wind}} \\ - \hat{p}_{w,t}^{\text{cur,adj}} - \omega_{w,t,s}) = P_{b,t}^{\text{d}} - \hat{p}_{b,t,s}^{\text{shed,adj}}, \quad \forall b \in \mathcal{B}, t \in \mathcal{T}, \end{aligned} \quad (13f)$$

$$\hat{p}_{w,t,s}^{\text{cur,adj}} \leq \hat{P}_{w,t}^{\text{wind}} - \omega_{w,t,s}, \quad \forall w \in \mathcal{W}, t \in \mathcal{T}, \quad (13g)$$

$$\hat{\tau}_{l,t,s} \geq \hat{A}_{l,t} (\hat{p}_{l,t,s}^{\text{adj}} + \xi_{l,t,s}) + \hat{B}_{l,t}, \quad \forall l \in \mathcal{L}^{\text{DLR}}, t \in \mathcal{T}, \quad (13h)$$

$$\hat{\tau}_{l,t,s} \geq -\hat{A}_{l,t} (\hat{p}_{l,t,s}^{\text{adj}} - \xi_{l,t,s}) + \hat{B}_{l,t}, \quad \forall l \in \mathcal{L}^{\text{DLR}}, t \in \mathcal{T}. \quad (13i)$$

The surrogate of the “wait-and-see” operation stage is formed to reflect the stochasticity in the “here-and-now” day-ahead UC. The surrogate corresponding (10a)–(10g) are (13a)–(13g), respectively. They all represent the same operational constraints, but the latter are not actual; they represent the constraints that are applied to scenarios. Thus, in (13f) and (13g),  $\omega_{w,t,s}$  represents the wind forecast error for each scenario. Equation (13h) and (13i) constrain  $\tau_{l,t,s}$  using the linear conductor-temperature approximation, as formulated in (2).  $\tau_{l,t,s}$  will be fixed to the lower bound as  $C_{l,t}^{\text{Dep}}$  is a convex function, working as a proxy of conductor temperature.  $\xi_{l,t,s}$  is the error of the DLR forecast, but instead of subtracting it from the DLR, we add it to the line flow.

The operation stage of a CHA-UC framework include an additional conductor depreciation cost term in the model. Other parts of the optimization problem are identical. The objective function of the CHA-UC real-time operation process is as follows.

$$\begin{aligned} \min_{\Xi} \sum_{t \in \mathcal{T}} \sum_{i \in \mathcal{I}} & \left[ C_i^{\text{P},2}(g_{i,t}^{\text{adj}})^2 + C_i^{\text{r}+} r_{i,t}^+ + C_i^{\text{r}-} r_{i,t}^- \right] \\ & + \sum_{t \in \mathcal{T}} \sum_{b \in \mathcal{B}} C^{\text{VoLL}} p_{b,t}^{\text{shed,adj}} + \sum_{t \in \mathcal{T}} \sum_{l \in \mathcal{L}^{\text{DLR}}} \underbrace{C_{l,t}^{\text{Dep}} (\tau_{l,t})}_{\text{Depreciation cost}}. \end{aligned} \quad (14)$$

The constraints identical to the baseline model are:

$$(10a) - (10g) \quad \text{Real-time operation,} \quad (15)$$

Additional conductor temperature related constraints are:

$$\tau_{l,t} \geq A_{l,t} \cdot p_{l,t}^{\text{adj}} + B_{l,t}, \quad \forall l \in \mathcal{L}^{\text{DLR}}, t \in \mathcal{T}, \quad (16a)$$

$$\tau_{l,t} \geq -A_{l,t} \cdot p_{l,t}^{\text{adj}} + B_{l,t}, \quad \forall l \in \mathcal{L}^{\text{DLR}}, t \in \mathcal{T}. \quad (16b)$$

The additional conductor temperature constraints enable the conductor temperature to be reflected in the objective function.

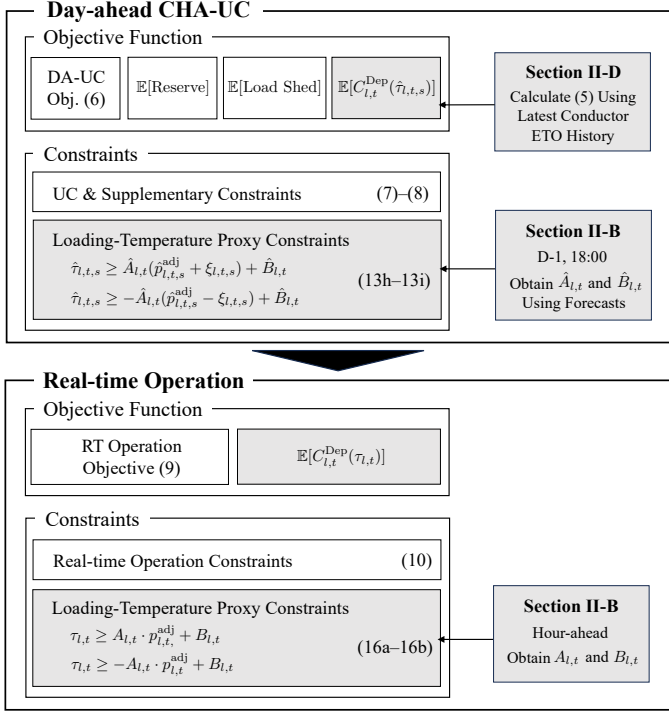


Fig. 4: Schematic of the CHA-UC optimization timeline. Processes that require actions outside optimization is colored with gray. Equations and factors are marked with its references.

### C. CHA-UC Timeline

The CHA-UC timeline is shown in Fig. 4. A UC problem is solved 18:00 the day before, and an operation problem is solved real-time (or hour-ahead). The loading-temperature linear fit should be updated everyday before the UC problem is solved to reflect the most recent conductor condition based on the latest forecasts. After operation, the depreciation cost function is updated for the next optimization period.

## IV. CASE STUDY

Two case studies are performed on the synthetic Texas 123-bus backbone transmission system (TX-123BT) [31] using 2021-2022 weather data. Case Study I runs an annual simulation with uncertain DLR forecasts (with errors) and perfect wind power (WP) forecasts (no errors) to illustrate CHA-UC. Case Study II evaluates CHA-UC in a more realistic setting with uncertainty in both WP and DLR forecasts to analyze their correlation effects.

### A. Preliminaries

1) *Simulation Settings:* In all case studies, a set of 21 lines was selected for DLR application<sup>1</sup>. All other lines used SLR limits. Each 345 kV line was modeled as ACSR Finch, and ampacity was adjusted to fit the TX-123BT system through a line multiplier. All optimization models were implemented in Julia/JuMP [32] and solved with Gurobi. The LoTS limit

<sup>1</sup>Lines were screened by solving an annual DCOPF with SLR and selecting those with the highest dual values of the line-flow constraint; lines longer than 100 km were excluded because their limits are dominated by stability.

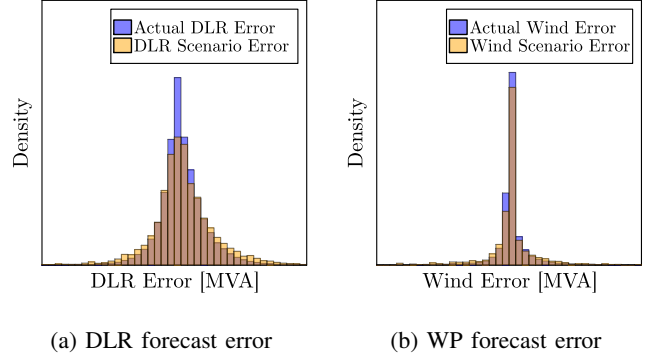


Fig. 5: Histograms comparing the distribution of actual and scenario errors. (a) DLR forecast error, (b) WP forecast error

was set to 10% (Section II-D). The lifetime cost factor  $B_l$  was based on a 3190 MVA, 400 kV AC line with a cost of 750 GBP/MVA-km [33]. After excluding tower and loss components, the adjusted cost factor ( $B_l$ ) was \$936/MVA-km. The loading-temperature linear fit was sampled from 95 °C and 195 °C, and the conductor depreciation piecewise function was sampled every 10 °C from 95 °C. For DLR security margin, line limits were constrained as  $K_{l,t} \hat{F}_{l,t}^{\text{DLR}} = \max(0.8 \hat{F}_{l,t}^{\text{DLR}}, F_l^{\text{SLR}})$ . The load profile of 2021 given in the TX-123BT test system was used, assuming no uncertainties in the load forecast. The value of lost load,  $C^{\text{VOLL}}$ , is assumed to be \$3500/MWh following MISO before 2025/05 [34]. Reserve activation costs followed [35]:  $C_i^{\text{r}+}$  equals three times, and  $C_i^{\text{r}-}$  equals 0.5 times, the linear cost coefficient of generator  $i$ .

2) *Data Collection:* Weather data for 2021–2022 were obtained from the NOAA’s high resolution rapid refresh model [36], which provides 3 km spatial resolution and 1 h temporal resolution. Forecasts issued at 18:00 the previous day were used as day-ahead inputs, while analysis data represented actual operation. Weather data from 2022 were used to generate stochastic scenarios, and 2021 data were used for annual simulations. WP profiles were derived from wind speeds using the standard power curve [37], adjusted to hub height via roughness-length correction. Uniform turbine specifications (cut-in and cut-out speeds) were assumed. For each transmission line, the hourly minimum DLR across all 3 km × 3 km grid cells intersecting the line corridor was used as the representative value. The parameters in (1) followed IEEE [26], with solar heat gain fixed at the worst-case condition for Texas (latitude 31°, 1000 W/m<sup>2</sup>, day 180, and maximum projected area). The conductor thermal limit was set to 95°C.

3) *Scenario Generation for CHA-UC:* To generate representative forecast-error scenarios for both WP and DLR while preserving their correlation, we construct a unified trajectory dataset where each record corresponds to one historical day and contains the 24-hour forecast errors. To ensure tail coverage, several historically extreme trajectories (large positive and negative errors) are first seeded. A greedy max–min selection then iteratively adds the trajectory with the largest minimum distance to the existing set, maximizing overall diversity. Finally, we assign probabilities via the nearest-

TABLE I. SUMMARIZED RESULTS OF CASE STUDY I AND CASE STUDY II. THE BEST RESULT FOR EACH COST IS IN **BOLD**.

Season	Method	Case Study 1 (no WP error)						Case Study 2 (with WP error)					
		Day-ahead Day Ahead [M\$/day]	Real-time Reserve [M\$/day]	Load Shed [M\$/day]	Post-hoc Dep. Cost [M\$/day]	DA+RT Curt. [MW/day]	Total [M\$/day]	Day-ahead Day Ahead [M\$/day]	Real-time Reserve [M\$/day]	Load Shed [M\$/day]	Post-hoc Dep. Cost [M\$/day]	DA+RT Curt. [MW/day]	Total [M\$/day]
Spring	CHA	14.32	0.13	—	0.27	11.5	<b>14.68</b>	14.70	<b>1.88</b>	<b>1.62</b>	<b>0.53</b>	104.6	<b>18.75</b>
	DLR	<b>14.17</b>	—	—	1.38	<b>10.3</b>	15.55	<b>13.73</b>	2.71	4.05	8.56	<b>79.6</b>	29.05
	SLR	14.57	—	—	<b>0.26</b>	83.8	14.89	14.15	2.28	2.91	5.52	94.9	24.87
Summer	CHA	29.96	0.13	—	<b>0.26</b>	20.1	<b>30.39</b>	29.75	<b>2.91</b>	<b>2.31</b>	<b>0.31</b>	49.6	<b>35.36</b>
	DLR	<b>29.59</b>	—	—	1.26	<b>3.4</b>	30.89	<b>28.43</b>	4.12	5.26	5.78	<b>31.9</b>	43.63
	SLR	29.92	—	—	0.85	64.5	30.80	28.79	3.67	4.20	5.65	33.8	42.36
Fall	CHA	22.10	0.08	—	<b>0.04</b>	<b>14.6</b>	<b>22.26</b>	22.00	<b>2.55</b>	<b>1.36</b>	<b>0.16</b>	74.6	<b>26.13</b>
	DLR	<b>21.82</b>	—	—	0.47	18.2	22.32	<b>20.87</b>	3.66	3.48	5.58	<b>47.6</b>	33.60
	SLR	22.23	—	—	0.06	108.2	22.33	21.13	3.27	2.52	5.30	81.3	32.38
Winter	CHA	18.53	0.06	—	0.23	<b>4.1</b>	<b>18.84</b>	18.65	<b>2.07</b>	<b>0.90</b>	<b>0.10</b>	63.7	<b>21.75</b>
	DLR	<b>18.39</b>	—	—	0.94	4.4	19.33	<b>17.71</b>	3.01	3.01	6.33	<b>41.7</b>	30.08
	SLR	18.86	—	—	—	51.2	18.89	18.14	2.61	2.10	4.42	60.0	27.28
Annual	CHA	21.25	0.09	—	<b>0.20</b>	12.7	<b>21.57</b>	21.30	<b>2.36</b>	<b>1.55</b>	<b>0.28</b>	73.2	<b>25.55</b>
	DLR	<b>21.02</b>	—	—	1.01	<b>9.1</b>	22.05	<b>20.21</b>	3.38	3.96	6.56	<b>50.3</b>	34.14
	SLR	21.42	—	—	0.30	77.1	21.74	20.61	2.96	2.94	5.23	67.5	31.77

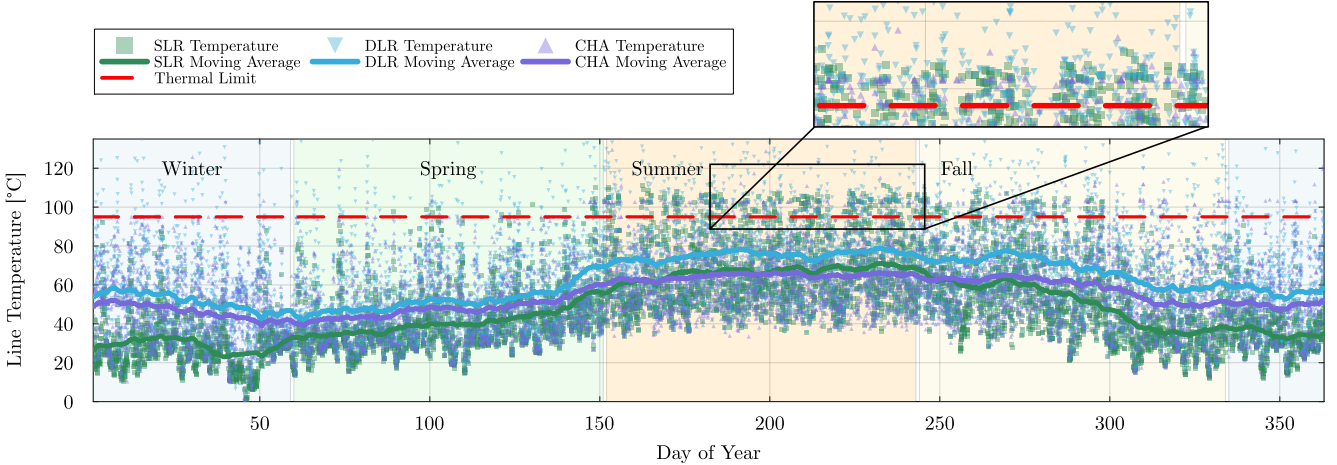


Fig. 6: (Case Study I) Annual scatter plot of temperatures of line 192 (Line with biggest temperature difference) obtained through post-hoc evaluation. 20-day moving average (MA) lines are drawn above. Meteorological seasons are colored in the background. A zoom-in of thermal overload temperatures during periods when the MA of SLR is higher than CHA-UC, is provided.

neighbor weighting: each historical trajectory is mapped to its closest selected scenario, and each scenario's probability equals the fraction of histories in its cell. This yields a scenario set that reflects the empirical distribution of forecast errors.

A total of 20 scenarios were generated from the historical data. Figure 5 shows that the resulting distribution slightly overestimates the empirical tails, ensuring adequate tail-risk representation. The correlation structure was also well preserved—the average empirical correlation was 0.04, compared to 0.05 across the generated scenarios—demonstrating effective reproduction of inter-asset dependencies.

#### B. Case study I - Value of Conductor Health Awareness

In case study I, wind forecast errors are neglected ( $\hat{P}_{w,t}^{\text{wind}} = P_{w,t}^{\text{wind}}$ ) and only DLR forecast errors are considered. This simplifies the risk structure and reduces the disparity between the day-ahead operation and the real-time operation, allowing for a clearer interpretation of the results. Also, the minimum online up-reserve requirement is set to zero, as this case study does not account for WP forecast errors.

*1) Overall Performance Comparison:* Table I presents a breakdown of the total cost of three models: baseline SLR, baseline DLR and CHA-UC. The units are normalized to one day. The day-ahead cost corresponds to the objective value of (6), which includes UC costs, fuel costs and the day-ahead load shedding costs.

CHA-UC achieves the lowest annual total cost of 21.57 M\$, reducing costs by 0.8% and 2.2% compared to the SLR and DLR baselines, respectively. This improvement reflects its ability to balance the risk of ETO against reduced operation costs. Although CHA-UC adopts DLR, it applies a conservative line flow than the baseline by accounting for expected conductor depreciation cost. As a result, the DLR baseline yields the lowest day-ahead cost, followed by CHA-UC and then SLR. WP curtailments are reduced by 88% (9.1 v.s. 77.1) when DLR is used instead of SLR, as it relieves grid congestion. CHA-UC retains part of this advantage, though its robustness discards some of it, leading to a 83% reduction (12.7 v.s. 77.1). On the other hand, depreciation costs were lowest for CHA-UC followed by SLR and DLR indicating that the CHA-UC preserves conductor lifespan most effectively.

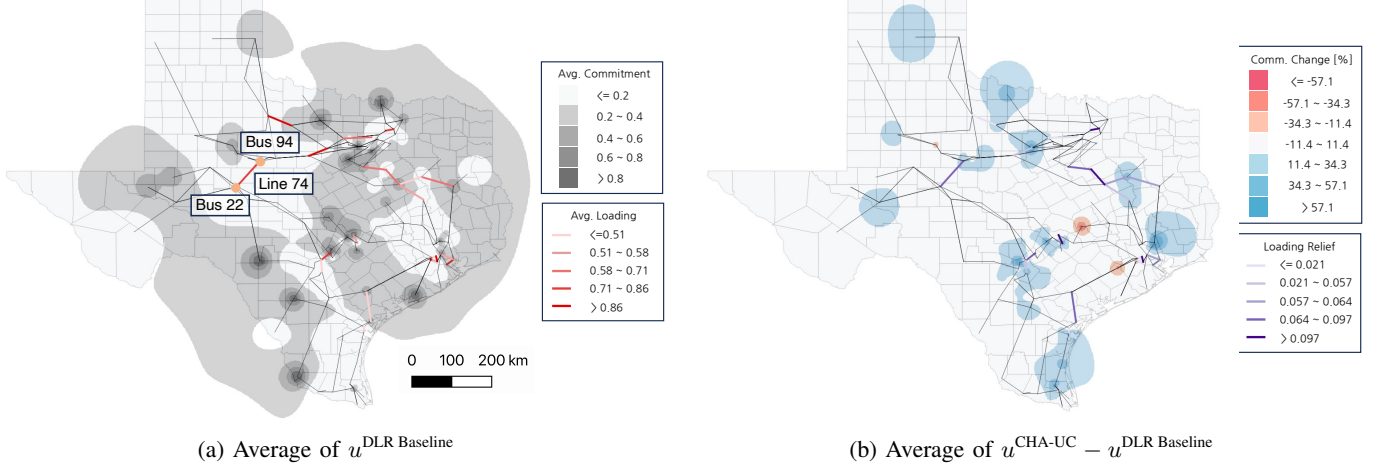


Fig. 7: (Case Study I) Annual heatmaps of day-ahead commitment and commitment changes on a map of Texas. (a) Annual day-ahead commitment from the DLR baseline, averaged over each bus; line colors indicate annual average loading (normalized by capacity). (b) Difference in commitment decisions in %; blue indicates higher commitment under CHA-UC. Line colors show the corresponding reduction in loading (normalized by capacity) when applying CHA-UC instead of the DLR baseline.

Finally, reserves are only activated in CHA-UC, as the SLR and DLR baselines involve no uncertainty in this case study.

2) *Risk of ETO*: Figure 6 visualizes the annual line temperature from the three models. In spring, fall and winter, the line temperatures were high in order of DLR baseline, CHA-UC and SLR baseline. This order originates from DLR not considering stochasticity with high ratings, CHA-UC considering stochasticity with high ratings, and SLR using a uniform low rating. However, during summer, the overall line temperatures increase and the temperature of SLR exceeds CHA-UC. This is because the hot operating conditions of summer increases the risk of SLR. Since summer weathers are close to the conservative conditions for SLR calculation, the “conservative” SLR becomes risky as well. Thus, CHA-UC chooses a more conservative loading, shown in the day-ahead cost of 29.96 M\$, which is higher than 29.92 M\$ of SLR baseline. A zoom-in of the scatter plot exhibits the results during this period. The temperatures from SLR was stamped more commonly over the thermal limit compared to CHA-UC, although CHA-UC has some outliers. This resulted in a CHA-UC depreciation cost of 0.26 M\$ which was 3.3 times and 4.8 times less than SLR and DLR baseline, respectively.

3) *Effect of CHA-UC to Commitment Decisions*: The annual average of commitment decisions made by DLR baseline is illustrated on a Texan map in Fig. 7(a). The cheapest units which comply with UC and DC PF constraints are committed, leading to aggressive line loading. The employment of CHA-UC leads to committing additional costly units to hedge the risks of ETO, leading to an overall relief of line loading in DLR lines, as presented in Fig. 7(b). For example, line 74, a key line connecting the south-west region and Dallas, is highly loaded in a direction to Dallas (Bus 22 to Bus 94) with an annual average of 83.5% (normalized by line capacity) when operated by DLR baseline. The transition to CHA-UC led to a 8.2% loading relief. This contributes to an annual conductor health relief of 16.2%, which translates to a 13.3 M\$ reduction in depreciation costs. Here, the commitment decisions took a

major role; the average commitment on bus 94 increased by 22%, and the commitment on bus 30, adjacent to the east of bus 94, increased by 28%, leading to the reduction of power flow to Dallas and the stress on line 74.

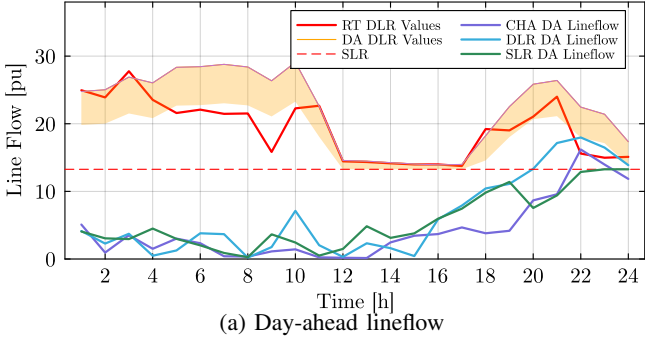
### C. Case study II - Impact of Correlated Forecast Errors

Case study 1 has shown the value of conductor health awareness. Case study 2 involves adding WP forecast errors. To handle wind generation forecast errors, a minimum reserve constraint of 5 GW (95% VaR of 2022 WP forecast error) is enforced.

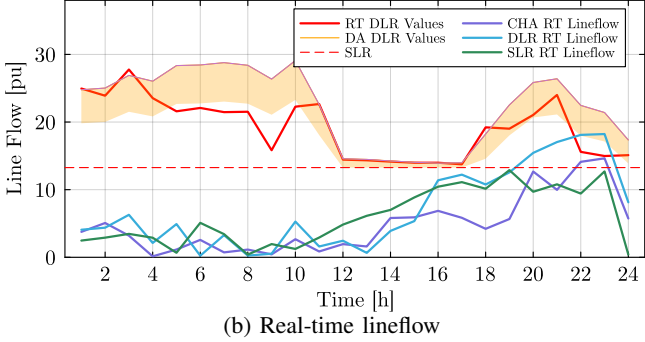
1) *Overall Performance Comparison*: The costs of the annual simulation are loaded on the right-hand side of Table I. Overall, the trend of the three models from case study I was preserved. CHA-UC recorded the lowest annual total cost, 25.5 M\$, contributing to a 25.2% and 19.8% reduction compared to DLR and SLR, respectively. However, unlike case study I, CHA-UC always incurred the highest day-ahead cost and it recorded the least reserve activation costs. This occurs as only CHA-UC accounts the stochasticity in WP forecasts in the day-ahead decision making.

2) *Impact of WP forecast error*: Figure 8 depicts how WP forecast errors affect line flow and conductor depreciation. In the day-ahead UC problem, the line flow is limited to stay under the security margin  $K_{l,t}$  of DLR forecasts. CHA-UC keeps a conservative DA line flow compared to DLR baseline by considering the stochasticity of DLR and WP forecasts, presented in Fig. 8(a). When the actual values of WP and DLR take effect, the real-time operation model deploys reserve to keep the power balance, creating fluctuations in the line flow shown in Fig. 8(b).

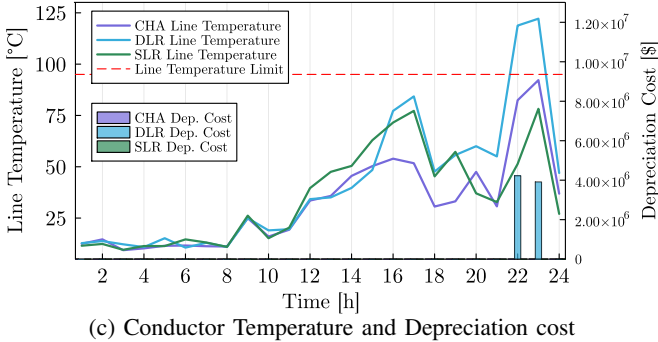
In hour 22, the actual DLR values were much lower than the forecast, causing ETO for DLR baseline. On the other hand, in hour 23, the RT line flow of DLR baseline surpassed the security margin of the DA DLR forecast, due to generation adjustments to balance WP forecast errors. In hour 23, WP



(a) Day-ahead lineflow



(b) Real-time lineflow



(c) Conductor Temperature and Depreciation cost

Fig. 8: (Case Study II) Lineflow, temperature and depreciation cost of line 74 at day 60 from baseline SLR, DLR and CHA-UC. (a) the day-ahead lineflow. Day-ahead DLR values and the security margin are colored orange. (b) real-time lineflow, obtained as a result of the operation stage. (c) The resultant conductor line temperature in lines and depreciation costs in bars, obtained through post-hoc analysis.

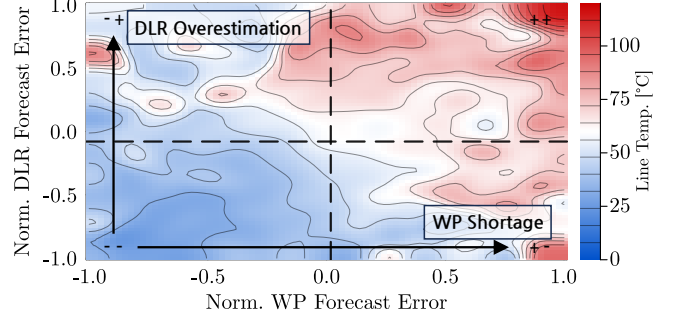
and DLR forecast errors combined unfavorably to amplify the depreciation. The line temperature and depreciation cost due to RT line flow in Fig. 8(c) visualize the impact of DLR and WP forecast errors. Counterintuitively, the temperature and depreciation costs are reversed in the two hours. This happens due to the diminishing depreciation cost, displayed in Fig. 3; the conductor loses sensitivity to ETO after high-temperature annealing.

3) *Impact of Correlated WP and DLR Forecast Error:* Five out of total six inter-asset correlations appeared from adjacent lines and wind farms. Two pairs of adjacent wind farms and lines were selected for deeper analysis. Table II lists the pairs; the two pairs have same signs of 1) correlation coefficients and 2) generation shift factor (GSF) of the WP bus to the line, but have different signs of average lineflow.

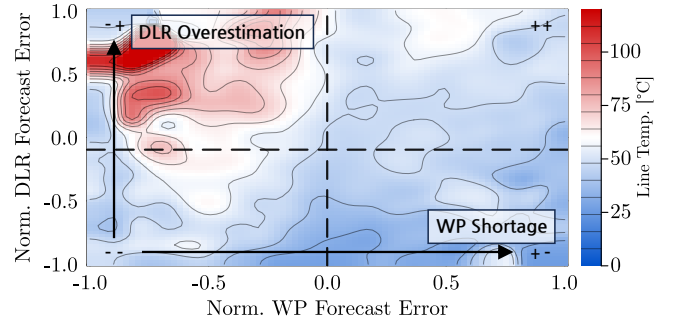
Figure 9 illustrates the heatmap of line temperature under baseline DLR. Forecast errors are calculated by subtracting

TABLE II. (CASE STUDY II) PAIRS OF CORRELATED WIND GENERATORS AND LINES STUDIED. THE CORRELATION WAS CAPTURED USING SPEARMAN'S CORRELATION COEFFICIENTS AND THE AVERAGE LINE FLOW USING DLR BASELINE IS GIVEN. GSF WAS OBTAINED BY SETTING THE PAIRED BUS AS THE FROM-BUS.

Pair	Wind Farm	Line	Correlation	GSF	Avg. Lineflow [pu]
1	8	74	0.38	0.26	-10.3
2	35	252	0.35	0.32	9.0



(a) Pair 1 (WP at Bus 22 and DLR on Line 74)



(b) Pair 2 (WP at Bus 120 and DLR on Line 252)

Fig. 9: (Case Study II) Heatmap of line temperatures under baseline DLR, given normalized WP and DLR forecast errors. Quadrants are indicated with pluses and minuses. a) Pair 1, b) Pair 2

actual values from the forecast value, meaning that a larger forecast error represents a larger overestimation of the value. Since the GSF is positive in pair 1, the shortage of WP leads to a reduction of line flow. The negative line flow becomes smaller, leading positive WP forecast error (shortage) to stress the conductor thermal limit. WP forecast errors are often hedged by the DLR forecast errors. The underestimation of DLR leads to an offset, where the WP shortage in the fourth quadrant is covered by the abundant line capacity. The first quadrant becomes risk-intensive due to the aggravation of DLR overestimation. Conversely, for pair 2, negative WP forecast errors (abundance) stress the conductor thermal limit, leading the second quadrant to be risk-intensive.

The positive correlation of the pairs causes the forecast error to occur more often in the first and third quadrants. Therefore, pair 1 becomes risk-prone, as the risk is dense in the first quadrant, and pair 2 becomes risk-averse, as the risk is dense in the second quadrant. This leads to a critical conclusion: the risk of positive forecast error correlation between WP and DLR is amplified when the GSF and average lineflow have

TABLE III. (CASE STUDY II) ANNUAL AVERAGE CHA-UC DAY-AHEAD LINEFLOWS BEFORE AND AFTER REMOVING CORRELATION FROM THE SCENARIO SET

Pair	CHA-UC [pu]	CHA-UC w/o Corr. [pu]	Conservativeness
1	-4.96	-5.23	Decreased
2	7.96	6.70	Increased

a different sign, and the risk is hedged when they have a same sign. The emergent property due to correlation should be considered for DLR operation.

An experiment regarding correlation proves that the CHA-UC is successfully reflecting the emergent effect of correlation. The scenario indices of the pairs were scrambled, changing the marginal minimally, so that the correlation of the scenarios becomes close to 0. This will lead to the inconsideration of correlation. Separate experiments done with two pairs, revealed in Table III, show that the original (correlation-considering) CHA-UC has kept a less conservative line flow for the risk-prone pair 1 and a more conservative line flow for the risk-hedging pair 2. This asserts that the CHA-UC successfully handles the effect of correlation.

## V. CONCLUSION

This paper presents CHA-UC, a stochastic unit commitment problem that considers line depreciation from ETO, effective for DLR operation. The CHA-UC optimization contains a conductor temperature estimation module and a conductor depreciation cost function to co-optimize the operation cost and depreciation cost. In result, case studies showcase a 0.8% and 83% reduction of total costs and WP curtailments compared to SLR operation, respectively. DLR operation without risk consideration showed highest costs due to the large conductor depreciation costs. The soundness of CHA-UC was proven by comparing annual line temperatures with the spatial commitment differences. A correlation analysis of DLR and WP forecast errors reveals the emergent properties from interactions of correlation, GSF and line flow. CHA-UC handles this properly. The statistics and analysis provided in the case studies will be important resources for DLR integration. The computational simplicity of the conductor temperature linear approximation will pay off. Despite some assumptions, our model proves to be most effective in the day-ahead operation with DLR, and provides meaningful materials for future grid research.

## ACKNOWLEDGEMENT

The authors would like to thank Baptiste Rabecq and Andy Sun at the Massachusetts Institute of Technology for insightful discussions that sparked the initial idea for this work.

## REFERENCES

- [1] S. Impram *et al.*, “Challenges of renewable energy penetration on power system flexibility: A survey,” *Energy Strategy Reviews*, 2020.
- [2] L. Herding *et al.*, “Assessing the impact of renewable energy penetration and geographical allocation on transmission expansion cost,” *Sustainable Energy, Grids and Networks*, vol. 38, p. 101349, 2024.
- [3] P. Donohoo-Vallett *et al.*, “Capricious cables: Understanding the limitations and context of transmission expansion planning models,” *The Electricity Journal*, vol. 28, no. 9, pp. 85–99, 2015.
- [4] L. Clapin *et al.*, “Waiting to generate: An analysis of onshore wind and solar pv project development lead-times in australia,” *Energy Economics*, vol. 131, p. 107337, 2024.
- [5] Potomac Economics, “2024 state of the market report for the ercot electricity markets,” Market Monitoring Report, May 2025.
- [6] S. Park, “Delays in grid build-out push renewable energy developers’ losses past ₩10 trillion,” *Kyunghyang Shinmun*, Oct. 2023.
- [7] C. J. Wallnerstrom *et al.*, “Impact from dynamic line rating on wind power integration,” *IEEE Transactions on Smart Grid*, 2015.
- [8] T. Lee *et al.*, “Impacts of dynamic line ratings on the ercot transmission system,” in *Proc. North Amer. Power Symp. (NAPS)*, 2022.
- [9] FERC, “Implementation of dynamic line ratings,” Washington, DC, Advance notice of proposed rulemaking RM24-6-000, Jun. 2024.
- [10] FERC, “Managing transmission line ratings,” Washington, DC, Final Rule (Order No. 881) RM20-16-000, Dec. 2021.
- [11] M. A. Bucher *et al.*, “Probabilistic n-1 security assessment incorporating dynamic line ratings,” in *2013 IEEE Power & Energy Society General Meeting*, 2013, pp. 1–5.
- [12] N. Viafora *et al.*, “Chance-constrained optimal power flow with non-parametric probability distributions of dynamic line ratings,” *International Journal of Electrical Power & Energy Systems*, 2020.
- [13] C. Wang *et al.*, “Risk-based distributionally robust optimal power flow with dynamic line rating,” *IEEE Trans. on Pwr. Syst.*, 2018.
- [14] H. Park *et al.*, “Stochastic security-constrained unit commitment with wind power generation based on dynamic line rating,” *Int. J. Electr. Power Energy Syst.*, 2018.
- [15] A. Kirilenko *et al.*, “Risk-averse stochastic dynamic line rating models,” *IEEE Transactions on Power Systems*, 2021.
- [16] M. Kim *et al.*, “Probabilistic dynamic line rating forecasting with line graph convolutional LSTM,” available in ArXiv.
- [17] K. Adomah *et al.*, “Probabilistic assessment of the reduction in tensile strength of an overhead transmission line’s conductor with reference to climatic data,” *IEEE Transactions on Power Delivery*, 2000.
- [18] J. R. Harvey, “Effect of elevated temperature operation on the strength of aluminum conductors,” *IEEE Trans. Power App. Syst.*, 1972.
- [19] P. Musilek *et al.*, “Spatial analysis of thermal aging of overhead transmission conductors,” *IEEE Transactions on Power Delivery*, 2012.
- [20] Electric Power Research Institute (EPRI), “Increased power flow guide-book: Increasing power flow in transmission and substation circuits,” Palo Alto, CA, Tech. Rep. 1010627, Nov. 2005.
- [21] PJM Interconnection, “Guide for determination of bare overhead transmission conductors,” Guidance Document, Dec. 2022.
- [22] J. Teh *et al.*, “Risk-based management of transmission lines enhanced with the dynamic thermal rating system,” *IEEE Access*, vol. 7, pp. 76 562–76 572, 2019.
- [23] K. Morozovska *et al.*, “A framework for application of dynamic line rating to aluminum conductor steel reinforced cables based on mechanical strength and durability,” *International Journal of Electrical Power & Energy Systems*, vol. 116, p. 105491, 2020.
- [24] B. O. Ngoko *et al.*, “Optimal power flow considering line-conductor temperature limits under high penetration of intermittent renewable energy sources,” *Int. J. Electr. Power Energy Syst.*, 2018.
- [25] J. Dai *et al.*, “An ADMM approach for unit commitment with considering dynamic line rating,” *Frontiers in Energy Research*, 2024.
- [26] “IEEE standard for calculating the current-temperature relationship of bare overhead conductors,” *IEEE Std 738-2023*, pp. 1–56, 2023.
- [27] R. Kluge, “Overhead transmission line ampacity ratings,” American Transmission Company, Technical Standard, Apr. 2012.
- [28] P. Brown *et al.*, “Hourly dynamic line ratings for existing transmission across the contiguous united states (preliminary results),” 2024.
- [29] Midcontinent Independent System Operator (MISO), “Transmission line ratings workshop: Typical industry practices,” Jan. 2021.
- [30] G. Morales-España *et al.*, “Tight and Compact MILP Formulation for the Thermal Unit Commitment Problem,” *IEEE Transactions on Power Systems*, vol. 28, no. 4, pp. 4897–4908, 2013.
- [31] J. Lu *et al.*, “A synthetic texas power system with time-series weather-dependent spatiotemporal profiles,” 2023, available in ArXiv.
- [32] M. Lubin *et al.*, “JuMP 1.0: Recent improvements to a modeling language for mathematical optimization,” *Mathematical Programming Computation*, 2023.
- [33] Parsons Brinckerhoff, “Electricity transmission costing study: An independent report endorsed by the institution of engineering & technology,” Institution of Engineering & Technology, Independent Report, Jan. 2012.
- [34] D. S. Kirschen and G. Strbac, *Fundamentals of Power System Economics*, 2nd ed. Hoboken, NJ: John Wiley & Sons, 2018.
- [35] V. Dvorkin, “Regression equilibrium in electricity markets,” *IEEE Transactions on Energy Markets, Policy and Regulation*, 2025.

- [36] S. G. Benjamin *et al.*, "A north american hourly assimilation and model forecast cycle: The rapid refresh," *Monthly Weather Review*, vol. 144, no. 4, pp. 1669–1694, Apr. 2016.
- [37] P. Giorsetto *et al.*, "Development of a new procedure for reliability modeling of wind turbine generators," *IEEE Transactions on Power Apparatus and Systems*, vol. PAS-102, no. 1, pp. 134–143, 1983.